Journal of Materials Chemistry A

ROYAL SOCIETY OF CHEMISTRY

PAPER

View Article Online
View Journal | View Issue

Cite this: J. Mater. Chem. A, 2022, 10, 17614

PtNi@ZIF-8 nanocatalyzed high efficiency and complete hydrogen generation from hydrazine borane: origin and mechanistic insight†

Changlong Wang,[a] Xiang Liu,[b] Yufeng Wu*[a] and Didier Astruc*[c]

The rational design of highly efficient nanocatalysts and understanding of the hydrogen generation process for selective and complete decomposition of hydrazine borane (HB) remain challenging. Here, a series of monodispersed, ultrasmall, highly efficient Pt_xNi_y alloyed nanoparticles were prepared using ZIF-8 as the MOF template. Upon scrutinizing the optimal Pt, Ni and support proportions, remarkable synergy of volcano-type is disclosed between these two metals in their alloy and with the ZIF-8 support. The high catalyst efficiency with complete gas evolution is among the best ever recorded, also showing promising utilization of this catalyst in other tandem reactions involving hydrogen. The experimental and DFT simulation results indicate that alloying Pt with Ni in PtNi@ZIF-8 with an optimized surface d-band center optimizes absorption and activation of the HB molecule, thereby reducing the energy barrier of the hydrolysis of the BH_3 group in HB. By systemically comparing the hydrolytic decomposition processes of HB over the nanocatalysts PtNi@ZIF-8 and RhNi@ZIF-8, the desorption of the borate is identified as the rate-determining step. In the following decomposition of the N_2H_4 moiety, the nanocatalyst PtNi@ZIF-8 always shows a smaller Gibbs free energy gap than RhNi@ZIF-8, rationalizing the faster kinetics for complete hydrogen evolution. The principle and results generated in the present study should contribute to optimizing the design of highly efficient nanocatalysts for hydrogen generation from hydrogen storage materials.

Received 2nd June 2022
Accepted 29th July 2022

DOI: 10.1039/d2ta04411k

rsc.li/materials-a

Supported nanoparticle (NP) catalysts are an essential part of heterogeneous catalysis.[1–4] The NP size, shape and stabilizer/support are decisive in the final catalyst performances.[5–12] In this regard, metal organic frameworks (MOFs) are outstanding emerging porous nanomaterials that have shown great advantages over conventional supporting materials.† [2,13–16] MOFs confine and stabilize catalytically active metal NPs within their frameworks or/and on their surfaces. In this way, the nucleation and growth of NPs are controlled, thus preventing their aggregation and prolonging the catalyst stability.[17–22] On the other hand, MOFs usually have permanent porosities (high specific surface areas) and tunable pore sizes that ensure good NP dispersion. This allows exposing active sites and facilitates the accessibility of substrates to the active NP surface by reducing the diffusion resistance.[17–22] Moreover, the direct use of the nanoconfinement effect by MOFs also provides a facile method to prepare surfactant free and ultrafine NP/MOF nanocomposites, which is significant and crucial for the design of highly efficient heterogeneous catalysts. In this context, particular attention has been paid to zeolitic imidazolate frameworks (ZIFs), due to their ease and greenness of synthesis in aqueous solutions and extraordinary high thermal and chemical stabilities.[23–27]

Hydrogen (H_2) is considered as a green, clean energy source and has received considerable attention. H_2 is currently produced by water electrolysis (the reverse of the most useful fuel cell reaction). Most of the active research involves H_2 generation by the electrocatalyzed hydrogen evolution reaction (HER), water photo- or photoelectrochemical splitting, and extraction from or hydrolysis of a number of hydrogen-rich substrates. Each has its own merits and drawbacks; however, specifically, H_2 generation from H_2 storage materials takes the safety problem into account and provides a convenient and effective approach to address challenges toward the establishment of a H_2 economy.[28–32] Recently, hydrazine borane (HB, $N_2H_4BH_3$), a stable and safe solid at room temperature with very high hydrogen atom content (15.4 wt%) and high solubility in water, has been proposed as a promising candidate for H_2 storage and production.[33–36] Theoretically, complete HB

[a]Institute of Circular Economy, Faculty of Materials and Manufacturing, Beijing University of Technology, Beijing 100124, China. E-mail: wuyufeng3r@126.com
[b]College of Materials and Chemical Engineering, Key Laboratory of Inorganic Nonmetallic Crystalline and Energy Conversion Materials, Material Analysis and Testing Center, China Three Gorges University, Yichang, Hubei 443002, China
[c]ISM, UMR CNRS N° 5255, Université de Bordeaux, 351 Cours de la Libération, 33405 Talence Cedex, France. E-mail: didier.astruc@u-bordeaux.fr

† Electronic supplementary information (ESI) available. See https://doi.org/10.1039/d2ta04411k

dehydrogenation can release, upon hydrolysis, 5 equiv. H_2 and 1 equiv. N_2 (eqn (1)) *via* both hydrolysis of the BH_3 group (eqn (2)) and complete decomposition of the N_2H_4 moiety (eqn (3)).[37,38]

$$N_2H_4BH_3(s) + 3H_2O \rightarrow B(OH)_3(l) + N_2(g) + 5H_2(g) \quad (1)$$

$$N_2H_4BH_3(s) + 3H_2O \rightarrow B(OH)_3(l) + N_2H_4(l) + 3H_2(g) \quad (2)$$

$$N_2H_4(l) \rightarrow N_2(g) + 2H_2(g) \quad (3)$$

Thus, the effective gravimetric hydrogen storage capacity (GHSC) of the $N_2H_4BH_3$–$3H_2O$ system reaches up to 10.0 wt%, which is much higher than those of other hydrogen systems such as NH_3BH_3–$4H_2O$ (5.9 wt% H)[39–48] and $N_2H_4 \cdot H_2O$ (8.0 wt% H).[49–53] Therefore, these unique advantages make $N_2H_4BH_3$ more competitive than the previously widely studied NH_3BH_3 and $N_2H_4 \cdot H_2O$ systems. However, the incomplete and undesired decomposition of HB especially in the decomposition of the N_2H_4 moiety ($3N_2H_4 \rightarrow 4NH_3(g) + N_2(g)$) led to the formation of ammonia (NH_3), which is toxic to fuel cell catalysts.[54–56] Thus, selective, complete and highly efficient catalysts are highly desirable to make HB a safe and efficient H_2 storage material.

To date, although noble and noble metal-free catalysts have been essentially developed for the decomposition of HB,[57–62] most of them suffer from incomplete hydrogen selectivity, slow kinetics and poor stability. Therefore, the fabrication of novel catalysts that exhibit 100% hydrogen selectivity, high activity and prominent stability for H_2 generation from HB aqueous solution is highly called for. Improvements of the catalytic activity, selectivity, and conversion rate under mild conditions could potentially be achieved by alloying a noble metal (*e.g.*, Rh, Pt, or Ru) with a first-row transition metal,[52,63–69] for instance Ni, which is also known for its high efficiency in nanoanalyzed H_2 production.[70–72] Among many alloyed systems, the PtNi alloys appear to be the most efficient ones. Successful examples include the $Ni_{0.9}Pt_{0.1}$ alloy NPs on MIL-101,[52] graphene supported $Ni_{0.58}Pt_{0.42}$ nanocatalyst,[55] and NiPt–MoO_x nanoparticles supported on NH_2 functionalized N doped rGO,[60] These examples showed the high efficiency of PtNi systems, though the supporting matrix is crucial. With ZIF-8 as the support, triple synergetic effects are observed, showing a much greater improvement in the H_2 generation rate.[69] Beyond the support, enhanced catalytic performance was typically attributed to the synergy effect of the nanoparticles. Upon alloying, the modulation of the electronic state over the alloyed nanocatalyst also needs be adapted to the adsorption/desorption behaviors of the reaction intermediate species on the surface, defining the reaction activation energy barrier and thereby regulating the catalytic activity. However, the clarification of the role of a metal and its interaction with the substrate in an alloyed nanocatalyst is crucial, and in particular, the mechanism of nanocatalyzed H_2 production from the dehydrogenation of HB in water remains unclear. These challenges not only involve difficulties in the rational design of highly efficient nanocatalysts, but also question the practical use of H_2 storage materials.

In order to address these critical issues, we report here the synthesis of the nanocatalyst PtNi/zeolitic imidazolate framework (ZIF)-8, $[Zn\text{-}(MeIM)_2]_n$). Specific efforts are focused on PtNi nanoalloys that are easyily synthesized and monodispersed with tunable compositions using ZIF-8 as a support for highly efficient and selective hydrogenation production upon hydrolytic decomposition of HB. Experiments and theoretical calculations provide insights into the origin of the PtNi@ZIF-8 catalyst high efficiency and the mechanism of complete HB decomposition herewith. In addition, tandem highly efficient hydrogenation of 4-nitrophenol is also found to be possible for the PtNi@ZIF-8 catalyst using the *in situ* H_2 generated from HB.

Results and discussion

Synthesis and characterization of the nanocatalysts

We started our investigation by first synthesizing the high-purity HB. Both X-ray powder diffraction (XRD) and nuclear magnetic resonance (NMR) spectroscopy confirmed the high purity of HB (Fig. S1–S3†). Next, we synthesized the ZIF-8 nanomaterial in aqueous solution using a known rapid method with high yield.[65,66] The XRD data show the pure phase of the crystal pattern of ZIF-8, and the transmission electron microscopy (TEM) image shows the small size of the ZIF-8 nanocrystals (Fig. S4†). ZIF-8 NPs show a type-I isotherm in the N_2 adsorption measurement with a high BET surface area. This nanomaterial used as the support here is known to be stable under reflux conditions in either water or methanol for one day without change of its nanostructure.[65,66]

The surfactant-free alloyed PtNi NPs supported on ZIF-8 were synthesized by co-reduction of nickel chloride and platinum tetrachloride in the presence of ZIF-8 in aqueous solution using sodium borohydride as a reductant under argon (Fig. 1, Scheme and ESI†). The nanocatalysts were then collected by centrifugation, washed with water, dried and used for tests. A series of Pt_xNi_y@ZIF-8 nanocatalysts were synthesized by varying the molar ratios of the two metal precursors.

These nanocatalysts were characterized as follows. The morphologies of Pt_xNi_y NPs supported on ZIF-8 were investigated by TEM and high-angle annular dark-field scanning transmission electron microscopy (HADDF-STEM, ESI†). Taking PtNi@ZIF-8 as an example, the electron microscopy images of PtNi@ZIF-8 show that the PtNi NPs are highly dispersed into the framework of ZIF-8 with an average particle size of 1.8 ± 0.3 nm (Fig. 1a–c). No isolated NPs from ZIF-8 are observed, indicating a strong anchoring effect between the PtNi and the ZIF-8 matrix. Fig. 1d–g show the HAADF-STEM images for the PtNi@ZIF-8 nanocomposites and the related elemental mappings with Pt and Ni. Ni and Pt appear to be co-distributed in these NPs and homogeneously dispersed on the ZIF-8 support, further indicating the formation of alloyed PtNi NPs (Fig. 1g and h) and their distribution on the surface or/and on the inter channel of the ZIF-8 support. In this area, the EDX result suggests that the percentage of Pt and Ni is about 37.12 wt% : 62.88 wt%. Atomic absorption spectrometry, by which the total concentrations of Pt and Ni in the whole sample are determined, indicates that the amounts of Pt and Ni in PtNi@ZIF-8 are respectively

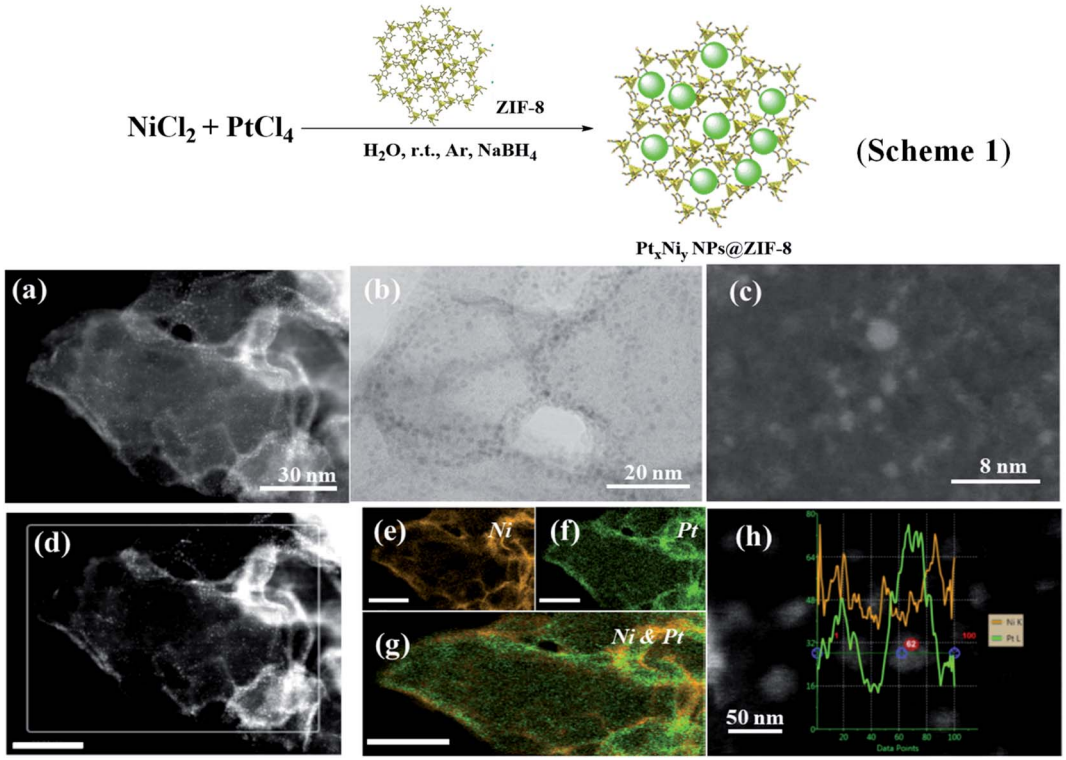

Fig. 1 General description of the synthesis of the nanocatalyst and characterization of the PtNi@ZIF-8 nanocatalyst. (a) HAADF-STEM image. (b) TEM image. (c) SE-STEM image. (d–g) HAADF-STEM image and element mapping images (scale bar 50 nm). (h) Line scan shows the PtNi nanoalloys.

5.68 wt% and 2.05 wt%, corresponding to a molar ratio of Pt and Ni of 1 : 1.2. These results are in agreement with the molar ratio of Pt and Ni with respect to the ratios used in the synthesis (molar ratio 1 : 1).

The XRD data show that all the nanocatalysts possess similar crystallinity and electronic structures (except Pt@ZIF-8), also similar to those of the ZIF-8 support. This suggests that the metal loadings in the present case are too low or the NPs are too small (Fig. S5†). On the other hand, with a much higher loading of Pt NPs, the Pt diffraction peaks in XRD matching the standard Pt peaks (JCPDS 04-0802) are clear (Fig. 2a and S13†). In comparison with the mother ZIF-8 support, all the nanocatalysts show type-I shapes and considerable decreases in both BET surface areas and pore volumes (Fig. 2b and Table S1†). For instance, the BET surface area and the pore volume of PtNi@ZIF-8 NPs decreased to 915.7 $m^2\ g^{-1}$ and 0.39 $cm^3\ g^{-1}$, respectively. This suggests blocking of the windows of the ZIF-8 framework cavities by highly dispersed PtNi NPs within the locally distorted environment or/and the location of PtNi NPs at the surface, as confirmed by electron microscope characterization (Fig. 1). Finally, *ex situ* XPS was employed to analyze the metal surface oxidation states. Binding energies (B.E.) of 70.6 and 73.9 eV were observed for Pt(0) $4f_{7/2}$ and Pt(0) $4f_{5/2}$, respectively (Fig. 2a). In addition, the B.E. value detected at 855.9 eV suggests a higher oxidation state than that of Ni(0) due to some unavoidable oxidation by air (Fig. 2b).[67–69,73]

Hydrogen production from the nanocatalyzed decomposition of HB

The catalytic activity of the prepared nanocatalysts for hydrolytic HB dehydrogenation was investigated at room temperature in aqueous solution. We first compared the effect of the NaOH concentration on the selectivity and activity in the hydrolytic HB dehydrogenation using the PtNi@ZIF-8 NP catalysts. This comparison demonstrated that the selectivity and activity of the catalysts for this HB dehydrogenation increased with the concentration of NaOH until this value reached 3 M. In all the cases, no ammonia was detected. A further increase of the amount of NaOH led to a decrease of activity (Fig. S14†). Control experiments showed that no gas was released from the reaction media in the absence of the catalyst, indicating that NaOH by itself had no effect on HB decomposition. Previous reports have suggested that NaOH served as a catalyst promoter for the decomposition of the N_2H_4 moiety in the second step of the reaction.[74,75] Our results have also confirmed this, because with the increase of NaOH concentration, the decomposition rate increased (Fig. S14†). The addition of NaOH also decreased the concentration of undesirable $N_2H_5^+$ ($N_2H_5^+ + OH^- \leftrightarrow N_2H_4 + H_2O$) and promote the deprotonation step ($N_2H_4 \rightarrow N_2H_3^* + H^*$) in the decomposition process of N_2H_4 (eqn (3)). On the other hand, the high concentration of alkaline solution also made the catalyst surface highly basic, which inhibited the formation of basic NH_3, beneficial for a high selectivity in H_2 evolution.[76]

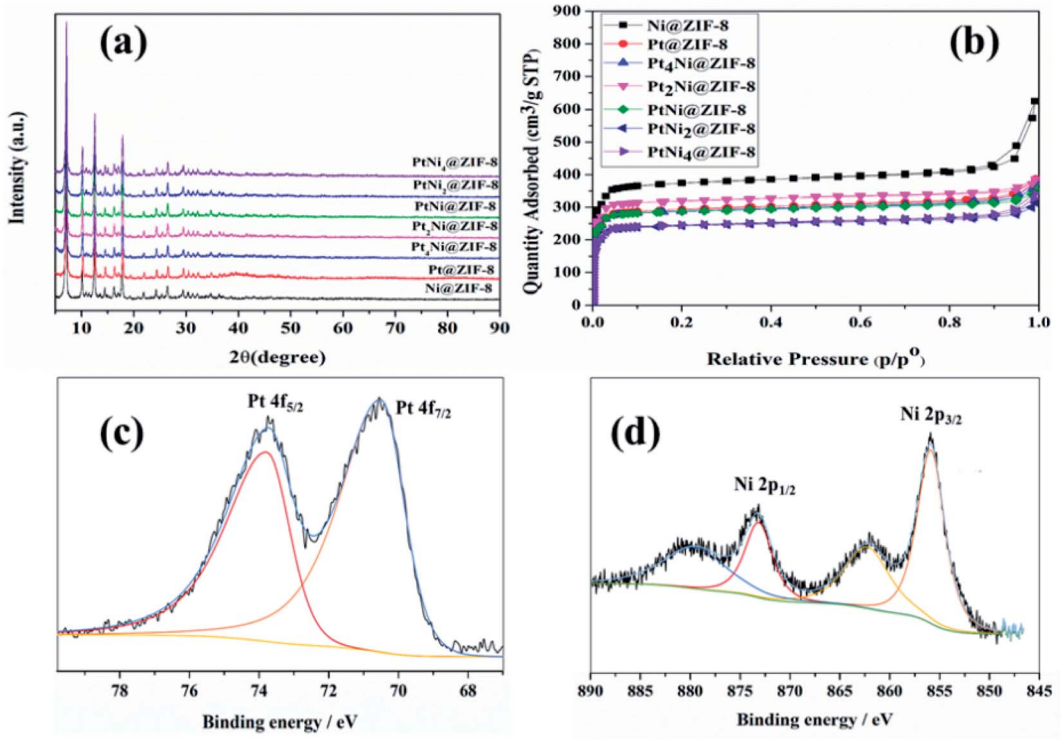

Fig. 2 (a) XRD spectra of the Pt_xNi_y@ZIF-8 nanocatalysts. (b) N_2 sorption isotherms. XPS spectra of (c) Pt 2p and (d) Ni 2p for the PtNi@ZIF-8 nanocatalyst.

We then tested the as-synthesized nanocatalysts with different Pt/Ni molar ratios for the HB decomposition in the presence of 3 M NaOH. Among all the catalysts, PtNi@ZIF-8 (*i.e.*, containing equal molar amounts of Ni and Pt) showed the best catalytic performance (Fig. 3a). Over the PtNi@ZIF-8 catalyst, 6.0 equiv. of gas (N_2 + H_2) were generated in only 9 min with a turnover frequency (TOF) of 572.4 h^{-1}; while over the catalysts $PtNi_4$@ZIF-8, $PtNi_2$@ZIF-8, and $PtNi_{0.5}$@ZIF-8, the reaction was

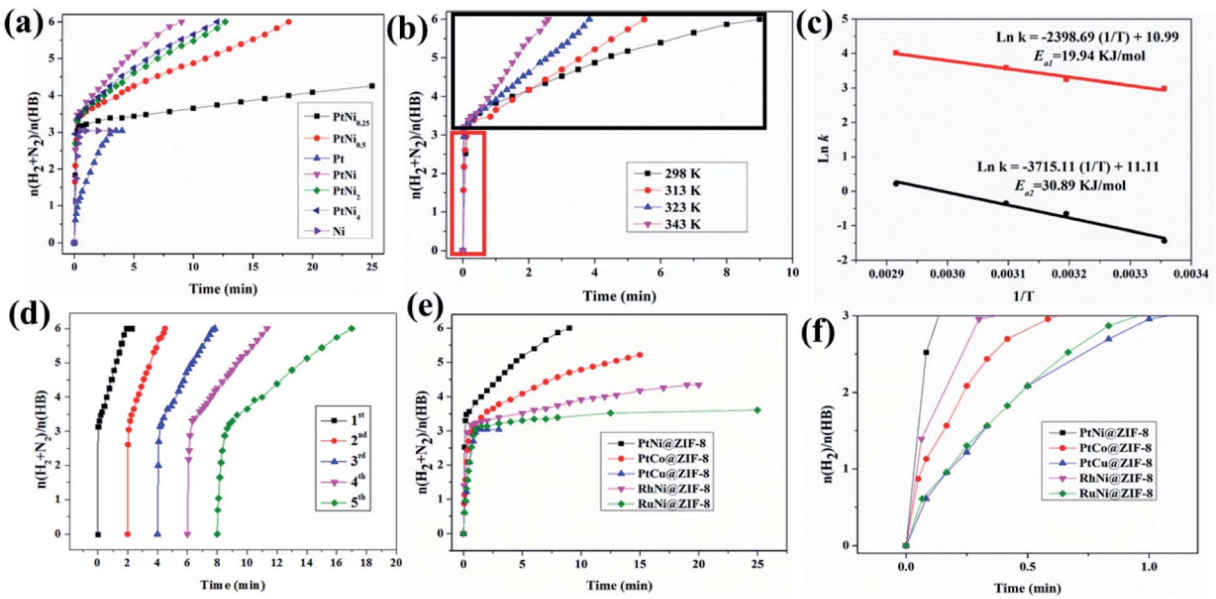

Fig. 3 (a) Time-course plots for the molar ratio of $n_{H2+N2}/n_{N2H4BH3}$ from decomposition of HB catalyzed by Pt_xNi_y@ZIF-8 nanocatalysts. (b) Time-course plots for the decomposition of HB catalyzed by PtNi@ZIF-8 at different temperatures, and (c) its related Arrhenius plots. (d) Recycle test of the PtNi@ZIF-8 nanocatalyst toward the decomposition of HB at 343 K. (e) Time-course plots for the decomposition of HB, and (f) the hydrolysis of BH_3 group over PtNi@ZIF-8, PtCo@ZIF-8, PtCu@ZIF-8, RhNi@ZIF-8 and RuNi@ZIF-8.

complete after 12, 12.7, and 18 min, corresponding to TOF values of 429.6, 405.9, and 286.4 h^{-1}, respectively. In the presence of the catalyst $PtNi_{0.25}$@ZIF-8, only 4.3 equiv. gas was released after 25 min, while the pure monometallic nanocatalysts were only effective for hydrolysis of the BH_3 moiety (*i.e.* releasing 3 equiv. H_2). The high efficiency and complete hydrolytic decomposition of HB using PtNi@ZIF-8 makes it one among the most efficient catalysts for this reaction (Table S2†).

In order to obtain the activation energy (E_a) of HB decomposition catalyzed by the nanocatalyst PtNi@ZIF-8, reactions were carried out at different temperatures, and the results are shown in Fig. 3b. Gas generation from HB decomposition was complete after 9, 5.5, 3.83, and 2.58 min at 298, 313, 323, and 343 K, respectively. The Arrhenius plot fitted on the basis of the TOF values for hydrolytic HB decomposition consists of the BH_3 group hydrolysis and the N_2H_4 moiety decomposition. The activation energies (E_a) were calculated for the both BH_3 group (E_{a1}) hydrolysis and N_2H_4 moiety decompositions (E_{a2}), which are 19.94 and 30.89 kJ mol^{-1}, respectively, showing that the BH_3 group is much easier to decompose than N_2H_4 (Fig. 3c). Thus, in the hydrolysis of HB, the improvement of the decomposition kinetics of N_2H_4 determines the final efficiency (*vide infra*). Moreover, in order to check the reusability and stability under high temperature of the catalyst, we reused the PtNi@ZIF-8 nanocatalyst at 343 K for the HB hydrolytic decomposition. As shown in Fig. 3d, the as-prepared nanocatalyst PtNi@ZIF-8 exhibited good recyclability, with a decrease in catalytic performance after the 5th run. After the reaction, XRD showed no change of the catalyst nanostructure. However, the TEM image suggests an increase in the PtNi NP size (Fig. S15†), and the BET surface area had decreased (Table S1†). The decrease of activity is ascribed to the increased NP size and the deactivation effect of the metaborate that accumulates at the catalyst surface during the hydrolysis of the BH_3 group of HB (*vide infra*).

The activities of other bimetallic nanoparticles supported on the same ZIF-8 support were also compared. A series of bimetallic nanoparticles, namely PtCo@ZIF-8, PtCu@ZIF-8, RhNi@ZIF-8, and RuNi@ZIF-8, were also synthesized under conditions identical to those used for the synthesis of PtNi@ZIF-8. The comparison of the activities is shown in Fig. 3e. Despite the differences in efficiency, incomplete decomposition of HB was observed in all these four other nanocatalysts, except PtNi@ZIF-8. Over the catalysts PtCo@ZIF-8, PtCu@ZIF-8, RhNi@ZIF-8 and RuNi@ZIF-8, the released gas ($N_2 + H_2$) was only 5.21, 3.04, 4.34, and 3.61 equiv., respectively. Thus, among these five catalysts, PtNi@ZIF-8 not only showed the highest activity, but also led to the complete hydrolytic decomposition of HB, confirming that PtNi shows the strongest synergistic effects in ZIF-8 according to the TOF values (*vide infra*). We also synthesized PtNi@SBA-15 and PtNi@UiO-66 (zirconium 1,4-dicarboxybenzene MOF) to investigate the synergistic effect with other supports (Fig. S16†). This comparison together with the data obtained with Ni@ZIF-8 and Pt@ZIF-8 in the hydrolytic decomposition of HB demonstrated that the best synergistic effect measured from the TOF values in the supported PtNi nanocatalysts is obtained with PtNi@ZIF-8 (Fig. 3a). The activity of PtNi on ZIF-8 is superior to that of either conventional SBA-15 supported PtNi or UiO-66 MOF supported PtNi, suggesting highly selective triple synergy between Ni, Pt and ZIF-8 in the catalytic hydrolytic decomposition of HB.

Origin of the high efficiency and mechanistic insight

The high efficiency and complete dehydrogenation of HB by PtNi NPs on various supports have already been demonstrated in the literature, and this is also confirmed by our experiments. However, since the support itself showed no catalytic activity for HB dehydrogenation, the main active site is derived from PtNi alloy. Indeed, despite the critical role of the ZIF-8 support, as we have compared its performance with the PtNi NPs supported on UIO-66 and SBA-15 (*vide supra*), the reason for the high efficiency and complete hydrolytic dehydrogenation of HB over PtNi NPs, beyond the support, remains unclear. To provide insights into the NP composition effect on the PtM/ZIF-8 (M = Ni, Co, and Cu) nanocatalyzed complete hydrogen generation from HB, we performed systematic density functional theory (DFT) calculations. Given the fact that the catalytic reaction occurs on the surface of the NPs, it is essential to check the adsorption of HB on the surface of the PtM NPs. Thus, the projected d-orbital density of states (DOS) of PtM was first studied to evaluate the d-band center position, which is intrinsically related with the metal-adsorbate binding strength.[77,78]

The projected d-orbital DOS at the (001) of those five nanocatalysts is thus calculated for comparison (Fig. 4). Generally, alloyed NPs show variations in the pDOS, signifying modification of electronic properties. As shown in Fig. 4a–c, the d-band center of the transition metal (M = Ni, Co, Cu) is closer to the Fermi level (E_F), indicating the preference of HB adsorption on the transition metal sites rather than on the Pt site.[79,80] Among all these three transition metals, Ni(001) showed the smallest d-band center (−1.18 eV) compared to Co(001) and Cu(001). Thus, upon alloying, the PtNi(001) surface has a higher d-band center than the monometallic counterpart Pt(001), suggesting that the d-states of PtNi are much closer to E_F compared to Pt. The upgrading of the d-band center energy level of PtNi indicates that the antibonding energy states increase, leading to stronger binding between the PtNi surface and the adsorbate species, HB.[79,80] The calculated adsorption energies for HB on the surface of PtM also support this conclusion (Fig. 4f); the adsorption energy of HB on PtNi is −2.84 eV, much stronger than that for HB on PtCo (−2.41 eV) and PtCu (−1.68 eV). Other comparisons also show similar effects of Ni to RhNi and RuNi. Thus, at the initial stage of the reaction, similar to the PtNi catalyzed hydrolysis of ammonia borane,[67–69,73] which has the same BH_3 group to be first dehydrogenated, the PtNi–HB activated species were formed through the stronger Pt–H bonds on the more electronegative surface site, Pt.[81] This is beneficial for the activation of the B–H bonds of the BH_3 group in HB, while the OH* radicals are trapped by the electron-deficient Ni surface.[82,83] In addition, the presence of abundant –OH groups near the Pt surface facilitates the rapid formation of the intermediates. Therefore, alloying Ni with the noble metals

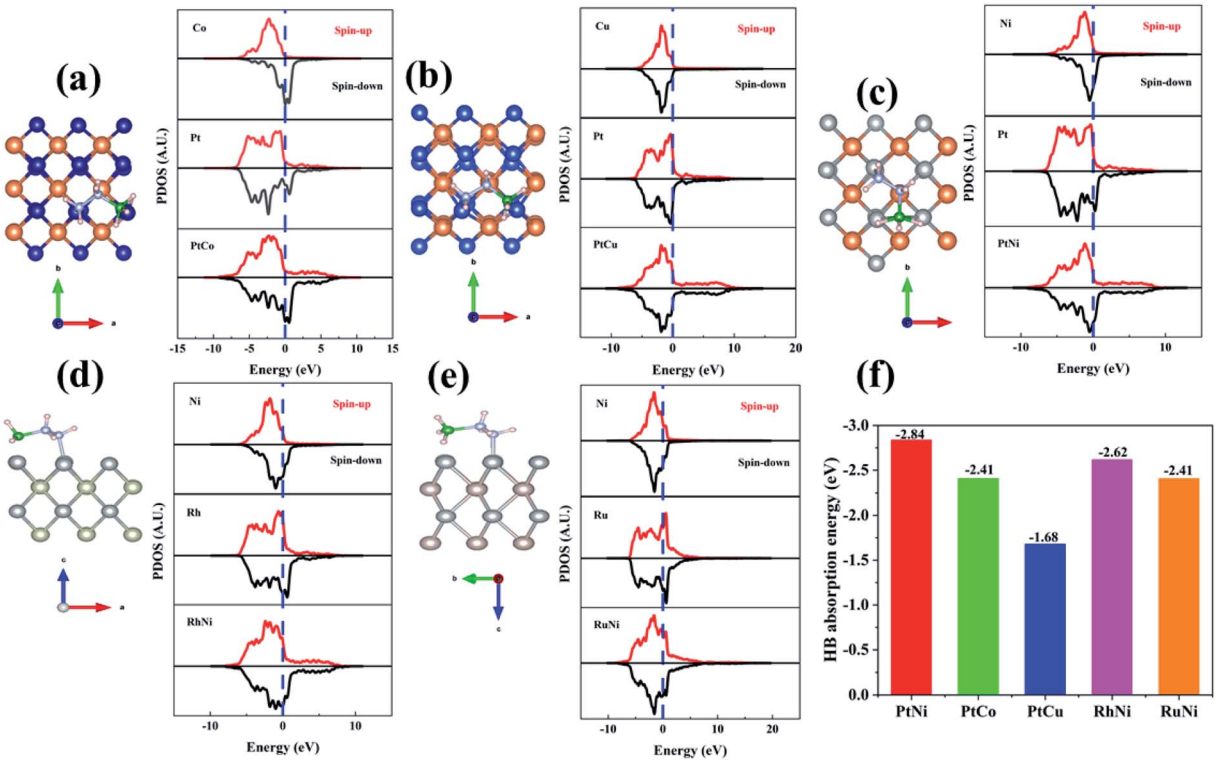

Fig. 4 (a–e) The top view and projected d-orbital DOS of PtCo(001), PtCu(001), PtNi(001), RhNi(001) and RuNi(001), respectively, and the E_F is set at 0 eV. (f) DFT-calculated adsorption energies for HB molecules on the (001) of the nanocatalysts. The brown, dark blue, blue, grey, light yellow, golden yellow, green, light red, and light-yellow balls represent Pt, Co, Cu, Ni, Rh, Ru, B, H and N, respectively.

promotes HB absorption and initial activation of the B–H bond of the BH_3 group in HB on the surface of the alloyed NPs. Thus, hydrolysis of the BH_3 group proceeds faster over alloyed NPs than over the monometallic counterparts (see Fig. 4).

Interestingly, except PtNi@ZIF-8, other Ni alloyed nanocatalysts (RhNi@ZIF-8 and RuNi@ZIF-8) do not catalyze complete hydrolytic dehydrogenation of HB under identical conditions. In the literature, this phenomenon was frequently observed, even if many other excellent supports were designed (see the survey, Table S2†). In order to clarify this aspect and provide insights into the reaction mechanism, we performed DFT calculations by choosing PtNi(001) and RhNi(001) as the typical examples to investigate the energy profiles for HB dehydrogenation processes at the atomic level.

The overall HB dehydrogenation process is divided into two basic steps, the hydrolysis of the BH_3 moiety and the dehydrogenation of the N_2H_4 moiety. As shown in Fig. 5 and S17,† in the presence of the nanocatalyst, the Gibbs free energy for the BH_3 hydrolysis is substantially decreased, while the decomposition of N_2H_4 is calculated with an energy increase. This confirms that the hydrolysis of the BH_3 group proceeds more rapidly than that of the N_2H_4 moiety in the dehydrogenation of HB,[59–64,74,75] which is in accordance with the experimental results and the literature. At the initial stage, HB is first adsorbed and activated on either PtNi(001) or RhNi(001). The activation energy for steps 1 and 2 is substantially decreased. Due to the differences in the Gibbs free energy of absorption and activation steps, the B–H bond in BH_3 is first cleaved on the surface of PtNi(001), releasing the first H_2 equiv. The step from $N_2H_4^*$ + BH_3^* to $N_2H_4^*$ + BH_2OH^* + $H_2(g)$ is thus decisive for this initial BH_3 hydrolysis process. Thereafter, the Gibbs free energy for the subsequent steps is decreased, releasing 3 equiv. of hydrogen. These calculations agree with the experimental results according to which the H_2 generation rate in the BH_3 hydrolysis catalyzed by PtNi@ZIF-8 is higher than that catalyzed by RhNi@ZIF-8 (Fig. 3e and f).

However, BH_3 hydrolysis also produces borates as side products, blocking the active sites of the nanocatalyst.[65–69,73,84,85] This leads to the deactivation of the catalyst for the following decomposition of the N_2H_4 moiety (*vide infra*). Therefore, the desorption of the borates $B(OH)_3^*$ to $B(OH)_3(g)$ in steps 5 and 6 is identified as the rate-determining step, which is calculated with the largest Gibbs free energy gap. The borates would quickly desorb on the surface of PtNi, while this seems to be more difficult on RhNi. Later, in every step of the decomposition of the N_2H_4 moiety, the Gibbs free energy increases, regardless of the catalyst type. However, the Gibbs free energy gap in each step of the decomposition of the N_2H_4 moiety over PtNi is always smaller than that over RhNi. As a result, the kinetics of the decomposition of the N_2H_4 moiety over RhNi becomes slow, and all these negative effects result in incomplete dehydrogenation of N_2H_4. Taken together, the nanocatalysts composed of PtNi have the advantages of better substrate adsorption, faster hydrolysis of BH_3 and desorption of the poisoning borate side

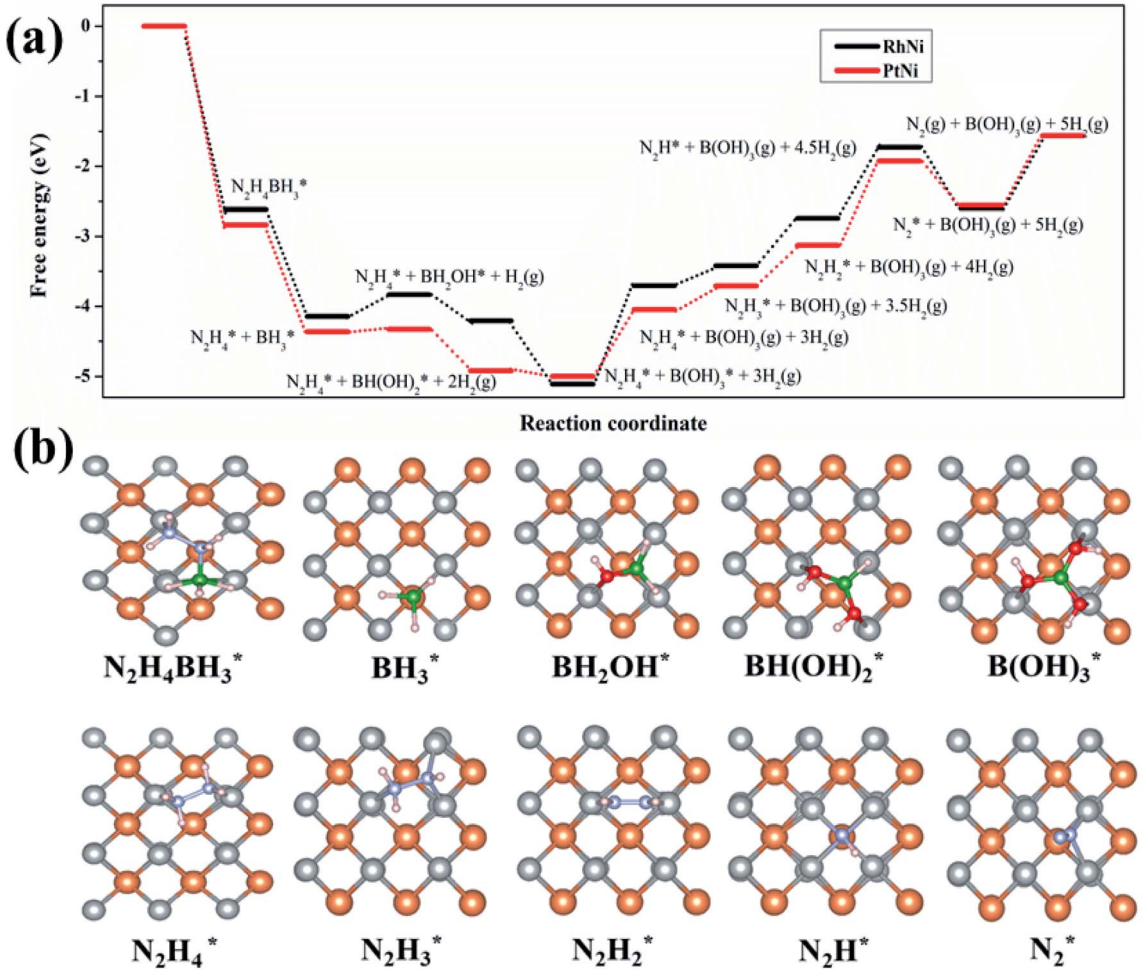

Fig. 5 (a) Calculated Gibbs free energy for H_2 generation from the decomposition of HB over the nanocatalysts PtNi@ZIF-8 and RhNi@ZIF-8. (b) Top view of the key intermediates generated from the HB decomposition over PtNi(001). The brown, grey, green, red, light red, and light-yellow balls represent Pt, Ni, B, O, H and N, respectively.

products, and better kinetics for N_2H_4 decomposition. Finally, overall performances towards highly efficient, selective and complete HB dehydrogenation are achieved in this way.

Previously, it has also been shown that ZIF-8/GO (graphene oxide) bi-supports showed a synergistic effect in the decomposition of formic acid.[86] In this case, GO modified the electronic structure of the supported NPs; thus the overall activity was greatly enhanced. In the hope of further increasing the efficiency, we first constructed the ZIF-8/GO bi-support and then deposited the PtNi NPs according to synthetic conditions that were the same as those used for the synthesis of PtNi@ZIF-8. PtNi@ZIF-8/GO presents a PtNi NP size similar to that of PtNi@ZIF-8. After testing the catalysis of these series of bi-support-deposited PtNi NPs in the decomposition of HB, however, a synergistic effect in the supports was not observed in the present study; the addition of different amounts of GO led to a decreased activity, and higher GO content resulted in incomplete hydrolytic decomposition of HB (Fig. S18†). Indeed, even the addition of 1 mg GO led to a sharp decrease of the BET surface areas (from 915.7 to 166.8 $m^2\ g^{-1}$). Thus, the negative synthetic effect was attributed to the decreased surface area and less exposed active sites.

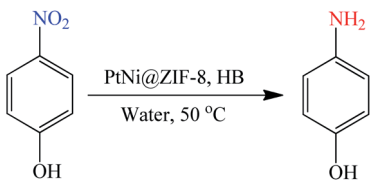

(4)

Finally, since HB is a promising hydrogen storage material, we for the first time propose that the *in situ* released hydrogen from HB can be used for tandem hydrogen reactions. As a proof of concept, following H_2 evolution, the reaction of 4-nitrophenol hydrogenation was performed using the nanocatalyst PtNi@ZIF-8 at 50 °C in aqueous solution (eqn (4)). 4-Nitrophenol is anthropogenic, toxic and inhibitory in nature, whereas its hydrogenation product 4-aminophenol is widely used as analgesic and antipyretic drugs, a photographic developer, a corrosion inhibitor, a anticorrosion lubricant, *etc.*[87] The yellow color of 4-nitrophenol disappeared within 1 min,

indicating full conversion to 4-aminophenol. This experiment demonstrated that the *in situ* generated H_2 from HB is potentially useful for hydrogenation reactions and that the catalyst PtNi@ZIF-8 is an efficient and versatile catalyst for hydrogenation reactions and presumably many other chemical reactions.

Concluding remarks

In summary, we have demonstrated that monodispersed, surfactant free, ultrasmall bimetallic PtNi nanocatalysts were synthesized using ZIF-8 as the MOF template. Upon scrutinizing the optimal amount of each metal proportion in the bimetallic catalyst, 100% hydrogen selectivity and high efficiency of H_2 evolution from HB aqueous solution were achieved with the reusable nanocatalyst PtNi@ZIF-8, which is one of the most efficient catalysts reported so far. This catalyst also advantageously compares with other compositions of noble-metal-containing bimetallic nanocatalysts using the same ZIF-8 support and other PtNi bimetallic catalysts using SBA-15 and UiO-66 supports. The high efficiency of the nanocatalyst PtNi@ZIF-8 is attributed to the ultrasmall size and highly selective triple synergy between Ni, Pt and ZIF-8.

Tandem hydrogenation of 4-nitrophenol was successfully conducted using the *in situ* generated H_2 from the potential H_2 storage material HB, showing high efficiency and versatility of this nanocatalyst. The experiments and theoretical calculations suggest the essential role of Ni in the nanocatalyst PtNi@ZIF-8 and the rate-determining borate desorption step in the highly efficient and complete hydrolytic HB decomposition.

The principles and results obtained here not only contribute to the rational design of bimetallic NP catalysts, but also potentially apply to many other chemical reactions for energy usage.

Conflicts of interest

There are no conflicts to declare.

Acknowledgements

Financial support from the National Key R&D Program of China (2021YFC2902505), the National Natural Science Foundation of China (No. 21805166), the start-up funding by Beijing University of Technology (C.W.) the 111 Project of China (No. D20015), the outstanding young and middle-aged science and technology innovation teams, Ministry of Education, Hubei province, China (T2020004), Foundation of Science and Technology Bureau of Yichang City (A21-3-012), University of Bordeaux and Centre National de la Recherche Scientifique (CNRS) is gratefully acknowledged. C.W. gratefully thanks Prof. F. Schüth (MPI-kofo) for his kind support.

References

1 L. Liu and A. Corma, *Chem. Rev.*, 2018, **118**(10), 4981–5079.
2 Thematic Issue: Nanoparticles in Catalysis. D. Astruc, *Chem. Rev.*, 2020, **120**(2), 461–463.
3 Thematic Issue: Heterogeneous Single-Atom Catalysis. J. Li, M. F. Stephanopoulos and Y. Xia, *Chem. Rev.*, 2020, **120**(21), 11699–11702.
4 Q. Yang, Q. Xu and H. −L. Jiang, *Chem. Soc. Rev.*, 2017, **46**, 4774–4808.
5 S. Navalon, A. Dhakshinamoorthy, M. Alvaro and H. Garcia, *Coord. Chem. Rev.*, 2016, **312**, 99–148.
6 M. K. Samantaray, V. D'Elia, E. Pump, L. Falivene, M. Harb, S. Ould-Chikh, L. Cavallo and J. M. Basset, *Chem. Rev.*, 2020, **120**, 734–813.
7 E. Gross, J. H.-C. Liu, F. D. Toste and G. A. Somorjai, *Nat. Chem.*, 2012, **4**, 947–952.
8 C. Bai and M. Liu, *Nano Today*, 2012, **7**, 258–281.
9 J. D. Scholden, B. C. Leal and J. Dupont, *ACS Catal.*, 2012, **2**, 184–200.
10 M. Sankar, N. Dimitratos, P. J. Miedjack, P. P. Wells, C. J. Kiely and G. J. Hutchings, *Chem. Soc. Rev.*, 2012, **41**, 8099–8139.
11 C. Amiens, D. Ciuculescu-Pradines and K. Philippot, *Coord. Chem. Rev.*, 2016, **308**, 409–432.
12 Y. Xia, K. D. Gilroy, H. −C. Peng and X. Xia, *Angew. Chem., Int. Ed.*, 2017, **56**, 60–95.
13 L. Zeng, X. Guo, C. He and C. Duan, *ACS Catal.*, 2016, **6**, 7935–7947.
14 J. Liu, L. Chen, H. Cui, J. Zhang, L. Zhang and C. −Y. Su, *Chem. Soc. Rev.*, 2014, **43**, 6011–6061.
15 A. H. Chughtai, N. Ahmad, H. A. Younus, A. Laypkov and F. Verpoort, *Chem. Soc. Rev.*, 2015, **44**, 6804–6849.
16 A. Dhakshinamoorthy and H. Garcia, *Chem. Soc. Rev.*, 2012, **41**, 5262–5284.
17 G. Lu, S. Li, Z. Guo, O. K. Farha, B. G. Hauser, X. Qi, Y. Wang, X. Wang, S. Han, X. Liu, J. SDuChene, H. Zhang, Q. Zhang, X. Chen, J. Ma, S. C. J. Loo, W. D. Wei, Y. Yang, J. T. Hupp and F. Huo, *Nat. Chem.*, 2012, **4**, 310–316.
18 B. Rungtaweevoranit, J. Baek, J. R. Araujo, B. S. Archanjo, K. M. Choi, O. M. Yaghi and G. A. Somorjai, *Nano Lett.*, 2016, **16**, 7645–7649.
19 K. M. Choi, D. Kim, B. Rungtaweevoranit, C. A. Trickett, J. T. D. Barmanbek, A. S. Alshammari, P. Yang and O. M. Yaghi, *J. Am. Chem. Soc.*, 2017, **139**, 356–362.
20 A. Aijaz, A. Karkamkar, Y. J. Choi, N. Tsumori, E. Rönnebro, T. Autrey, H. Shioyama and Q. Xu, *J. Am. Chem. Soc.*, 2012, **134**, 13926–13929.
21 M. Zhao, K. Yuan, Y. Wang, G. Li, J. Guo, L. Gu, W. Hu, H. Zhao and Z. Tang, *Nature*, 2016, **539**, 76–80.
22 B. An, J. Zhang, K. Cheng, P. Ji, C. Wang and W. Lin, *J. Am. Chem. Soc.*, 2017, **139**, 3834–3840.
23 Q. Wang and D. Astruc, *Chem. Rev.*, 2020, **120**(2), 1438–1511.
24 X. Li, X. Yang, H. Xue, H. Pang and Q. Xu, *EnergyChem*, 2020, **2**, 100027.
25 X. Yang and Q. Xu, *Trends Chem.*, 2020, **2**, 214–226.
26 G. Li, S. Zhao, Y. Zhang and Z. Tang, *Adv. Mater.*, 2018, **30**, 1800702.
27 B. Li, J.-G. Ma and P. Cheng, *Small*, 2019, **15**, 1804849.
28 T. He, P. Pachfule, H. Wu, Q. Xu and P. Chen, *Nat. Rev. Mater.*, 2016, **1**, 16059.

29 C. Lang, Y. Jia and X. Yao, *Energy Storage Mater.*, 2020, **26**, 290–312.
30 Q. Yao, Y. Ding and Z.-H. Lu, *Inorg. Chem. Front.*, 2020, **7**, 3837–3874.
31 C. Wang and D. Astruc, *Chem. Soc. Rev.*, 2021, **50**, 3437–3484.
32 X. Liu, X. Zhang, D.-S. Li, S. Zhang and Q. Zhang, *J. Mater. Chem. A*, 2021, **9**, 18164–18174.
33 J. Hannauer, O. Akdim, U. B. Demirci, C. Geantet, J.-M. Herrmann, P. Miele and Q. Xu, *Energy Environ. Sci.*, 2011, **4**, 3355–3358.
34 R. Moury, G. Moussa, U. B. Demirci, J. Hannauer, S. Bernard, E. Petit, A. van der Lee and P. Miele, *Phys. Chem. Chem. Phys.*, 2012, **14**, 1768–1777.
35 D. Celik, S. Karahan, M. Zahmakiran and S. Ozkar, *Int. J. Hydrogen Energy*, 2012, **37**, 5143.
36 T. Hugle, M. F. Kuhnel and D. Lentz, *J. Am. Chem. Soc.*, 2009, **131**, 7444–7446.
37 Q. L. Xu and Q. Xu, *Energy Environ. Sci.*, 2015, **8**, 478–512.
38 S. Zhang, Q. Yao and Z. Lu, *Prog. Chem.*, 2017, **29**, 426.
39 X. Wang, D. Liu, S. Song and H. Zhang, *J. Am. Chem. Soc.*, 2013, **135**, 15864–15872.
40 W. Chen, J. Ji, X. Feng, X. Duan, G. Qian, P. Li, X. Zhou, D. Chen and W. Yuan, *J. Am. Chem. Soc.*, 2014, **136**, 16736–16739.
41 J. X. Kang, T. W. Chen, D. F. Zhang and L. Guo, *Nano Energy*, 2016, **23**, 145–152.
42 M. A. Khalily, H. Eren, S. Akbayrak, H. H. Susapto, N. Biyikli, S. Özkar and M. O. Guler, *Angew. Chem., Int. Ed.*, 2016, **55**, 12257–12261.
43 O. Metin, V. Mazumder, S. Özkar and S. Sun, *J. Am. Chem. Soc.*, 2010, **132**, 1468–1469.
44 Y. Z. Chen, Q. Xu, S. H. Yu and H. L. Jiang, *Small*, 2015, **11**, 71–76.
45 C. Y. Peng, L. Kang, S. Cao, Y. Chen, Z. S. Lin and W. F. Fu, *Angew. Chem., Int. Ed.*, 2015, **54**, 15725–15729.
46 K. Feng, J. Zhong, B. Zhao, H. Zhang, L. Xu, X. Su and S. T. Lee, *Angew. Chem., Int. Ed.*, 2016, **55**, 11950–11954.
47 Q. L. Yao, Z. H. Lu, W. Huang, X. Chen and J. Zhu, *J. Mater. Chem. A*, 2016, **4**, 8579–8583.
48 Z. Li, T. He, L. Liu, W. Chen, M. Zhang, G. Wu and P. Chen, *Chem. Sci.*, 2017, **8**, 781–788.
49 S. K. Singh and Q. Xu, *J. Am. Chem. Soc.*, 2009, **131**, 18032–18033.
50 J. Wang, X. B. Zhang, Z. L. Wang, L. M. Wang and Y. Zhang, *Energy Environ. Sci.*, 2012, **5**, 6885–6888.
51 L. He, Y. Huang, A. Wang, X. Wang, X. Chen, J. J. Delgado and T. Zhang, *Angew. Chem., Int. Ed.*, 2012, **51**, 6191–6194.
52 Z. Zhang, S. Zhang, Q. Yao, X. Chen and Z. H. Lu, *Inorg. Chem.*, 2017, **56**, 11938–11945.
53 W. Kang and A. Varma, *Appl. Catal. B: Environ.*, 2018, **220**, 409–416.
54 Z.-J. Zhang, Z.-H. Lu, H.-L. Tan, X.-S. Chen and Q.-L. Yao, *J. Mater. Chem. A*, 2015, **3**, 23520–23529.
55 J.-M. Chen, Z.-H. Lu, W. Huang, Z.-B. Kang and X.-S. Chen, *J. Alloys Compd.*, 2017, **695**, 3036–3043.
56 N. Tunc, B. Abay and M. Rakap, *J. Power Sources*, 2015, **299**, 403–407.
57 S. Karahan and S. Ozkar, *Int. J. Hydrogen Energy*, 2015, **40**, 2255–2265.
58 K. Yang, Q. Yao, W. Huang, X. Chen and Z.-H. Lu, *Int. J. Hydrogen Energy*, 2017, **42**, 6840–6850.
59 S.-J. Li, H.-L. Wang, B.-R. Wulan, X.-B. Zhang, J. M. Yan and Q. Jiang, *Adv. Energy Mater.*, 2018, 1800625.
60 X. Kang, J. X. Yao, Y.-X. Duan, Z.-Y. Chen, J.-M. Yan and Q. Jiang, *J. Mater. Chem. A*, 2021, **9**, 26704–26708.
61 Q. Yao, Z.-H. Lu, R. Zhang, S. Zhang, X. Chen and H.-L. Jiang, *J. Mater. Chem. A*, 2018, **6**, 4386–4393.
62 S.-J. Li, X. Kang, B.-R. Wulan, X.-L. Qu, K. Zheng, X.-D. Han and J.-M. Yan, *Small Methods*, 2018, **2**, 1800250.
63 T. Karaca, M. Sevim and Ö. Metin, *ChemCatChem*, 2017, **8**, 4185–4190.
64 J. Chen, Z. H. Lu, Q. Yao, G. Feng and Y. Luo, *J. Mater. Chem. A*, 2018, **6**, 20746–20752.
65 C. Wang, J. Tuninetti, Z. Wang, C. Zhang, R. Ciganda, L. Salmon, S. Moya, J. Ruiz and D. Astruc, *J. Am. Chem. Soc.*, 2017, **139**, 11610–11615.
66 C. Wang, Q. Wang, F. Fu and D. Astruc, *Acc. Chem. Res.*, 2020, **53**(10), 2483–2493.
67 J. Zhang, W. Chen, H. Ge, C. Chen, W. Yan, Z. Gao, J. Gan, B. Zhang, X. Duan and Y. Qin, *Appl. Catal. B: Environ.*, 2018, **235**, 256–263.
68 J. Zhang, X. Zheng, W. Yu, X. Feng and Y. Qin, *Appl. Catal. B: Environ.*, 2022, **306**, 121116.
69 F. Fu, C. Wang, Q. Wang, A. M. Martinez-Villacorta, A. Escobar, H. Chong, X. Wang, S. Moya, L. Salmon, E. Fouquet, J. Ruiz and D. Astruc, *J. Am. Chem. Soc.*, 2018, **140**, 10034–10042.
70 Y. Yu, Y.-M. Gan, C. Huang, Z. H. Lu, X. Wang, R. Zhang and G. Feng, *Int. J. Hydrogen Energy*, 2020, **45**, 16528–16539.
71 C. Huang, H. Li, J. Yang, C. Wang, F. Hu, X. Wang, Z. H. Lu, G. Feng and R. Zhang, *Appl. Surf. Sci.*, 2019, **478**, 708–716.
72 M. Huang, Q. L. Yao, G. Feng, H. Zou and Z. H. Lu, *Inorg. Chem.*, 2020, **59**, 5781–5790.
73 Z. Gao, G. Wang, T. Lei, Z. Lv, M. Xiong, L. Wang, S. Xing, J. Ma, Z. Jiang and Y. Qin, *Nat. Commun.*, 2022, **13**, 118.
74 W. Wang, X. Hong, Q. Yao and Z.-H. Lu, *J. Mater. Chem. A*, 2020, **8**, 13694–13701.
75 X. Hong, Q. Yao, M. Huang, H. Du and Z. H. Lu, *Inorg. Chem. Front.*, 2019, **6**, 2271–2278.
76 Q.-L. Zhu, D.-C. Zhong, U. B. Demirci and Q. Xu, *ACS Catal.*, 2014, **4**, 4261–4268.
77 A. J. Medford, A. Vojvodic, J. S. Hummelshøj, J. Voss, F. Abild-Pedersen, F. Studt, T. Bligaard, A. Nilsson and J. K. Nørskov, *J. Catal.*, 2015, **328**, 36–42.
78 C. Wei, Y. Sun, G. G. Scherer, A. C. Fisher, M. Sherburne, J. W. Ager and Z. J. Xu, *J. Am. Chem. Soc.*, 2020, **142**, 7765–7775.
79 X. Zhang, Y. Zhao, X. Jia, Y. Zhao, L. Shang, Q. Wang, G. I. N. Waterhouse, L.-Z. Wu, C.-H. Tung and T. Zhang, *Adv. Energy Mater.*, 2018, **8**, 1702780.
80 Z. Chen, Y. Song, J. Cai, X. Zheng, D. Han, Y. Wu, Y. Zang, S. Niu, Y. Liu, J. Zhu, X. Liu and G. Wang, *Angew. Chem., Int. Ed.*, 2018, **57**, 5076–5080.

81 W. Li, Y. Zhao, Y. Liu, M. Sun, G. I. N. Waterhouse, B. Huang, K. Zhang, T. Zhang and S. Lu, *Angew. Chem., Int. Ed.*, 2021, **60**, 3290–3298.
82 Y. Liu, H. Wen, D. Zhou, X. Huang, X. Wu, J. Jiang, X. Guo and B. Li, *Appl. Catal. B: Environ.*, 2021, **291**, 120094.
83 P. Li, R. Chen, Y. Huang, W. Li, S. Zhao and S. Tian, *Appl. Catal. B: Environ.*, 2022, **300**, 120725.
84 Q. −L. Zhu, J. Li and Q. Xu, *J. Am. Chem. Soc.*, 2013, **135**, 10210–10213.
85 M. Rakap, *Appl. Catal., B*, 2015, **163**, 129–134.
86 J. M. Yan, Z. L. Wang, L. Gu, S. J. Li, H. L. Wang, W. T. Zheng and Q. Jiang, *Adv. Energy Mater.*, 2015, **5**, 1–6.
87 P. Zhao, X. Feng, D. Huang, G. Yang and D. Astruc, *Coord. Chem. Rev.*, 2015, **287**, 114–136.